Optimized Machine Learning Models for Predicting Compressive, Tensile, and Flexural Strengths of Multi-Fiber Recycled Aggregate Concrete

Journal of
*Composites Science*

MDPI

*Article*

# Optimized Machine Learning Models for Predicting Compressive, Tensile, and Flexural Strengths of Multi-Fiber Recycled Aggregate Concrete

**Marwah Al tekreeti *, Ali Bahadori-Jahromi, Shah Room and Zeeshan Tariq**

Department of Civil Engineering and Built Environment, School of Computing and Engineering, University of West London, London W5 5RF, UK; ali.bahadori-jahromi@uwl.ac.uk (A.B.-J.); shah.room@uwl.ac.uk (S.R.); zeeshan.tariq@uwl.ac.uk (Z.T.)

* Correspondence: marwah.altekreeti@uwl.ac.uk; Tel.: +44-7306144771

**Abstract**

The demand for concrete has led to increased use of raw materials and significant waste generation. Recycled aggregate concrete (RAC) offers a viable approach to sustainable concrete; however, the use of weakly bonded mortar on aggregate leads to low strength and crack formation. Fiber reinforcement, specifically hybrid fiber reinforcement combining steel, glass, basalt, and polypropylene fibers, can increase the tensile and flexural properties of RAC. This study developed machine learning models to enable the prediction of hybrid fiber-reinforced RAC's compressive, splitting tensile, and flexural strength performance; these new models overcome the limitations of previous research, which relied on only one fiber type and regular methods of optimization. Two models (a deep neural network (DNN) and an XGBoost model) were trained and optimized using bald eagle search (BES), particle swarm optimization (PSO), and the Bayesian optimization (BO) algorithm to improve performance. Among the three optimization analyses, PSO-XGBoost achieved the highest accuracy for compressive strength and splitting tensile strength, while BES-XGBoost achieved the highest accuracy for flexural strength. The most significant influences on the compressive strength were curing age and silica fume, while the main drivers of splitting tensile strength and flexural strength were fiber volume and fiber characteristics. The use of SHAP-based methodology with a user-friendly interface further improved the design of RAC mixtures, reducing waste from raw materials, enhancing the structural performance of RAC, and enabling data-driven decision-making in the manufacturing of eco-friendly concrete products.

**Keywords:** recycled aggregate concrete; fiber; machine learning; mechanical properties; hybrid fiber



Academic Editor: Junjie Zeng

Received: 26 January 2026
Revised: 11 February 2026
Accepted: 2 March 2026
Published: 6 March 2026



## 1. Introduction

A major increase in the demand for construction activities and development has shaped not only the consumption of natural resources and energy but also generated large amounts of construction and demolition waste (C&D). C&D waste is generated in large quantities every year, as evidenced by the United Kingdom, which produces over 59.4 million tons of C&D waste annually [1]. Also, the destruction from international conflicts and natural disasters generates millions of tons of rubble, underscoring the need to adopt effective waste management strategies. Recycled concrete aggregate (RCA) is a material used in the construction industry as a substitute for natural aggregate to address

environmental problems [2,3]. RCA is used in concrete production as an aggregate, providing a sustainable alternative that reduces the use of natural resources while simultaneously reducing waste. However, RCA also has reduced strength properties and is brittle in nature compared to natural aggregate due to the presence of old mortar left on the surface of the recycled aggregate, which comprises about 40% of the RCA material [4]. Recycled aggregate concrete (RAC) has a strength approximately 20% lower than that of natural aggregate concrete (NAC) [5]. Splitting tensile strength decreases by approximately 10%, and the elastic modulus drops by 40% relative to NAC properties [6–8].

A study conducted on RCA-reinforced concrete beam tests found that higher RCA content in tests reduced flexural and shear strength, beam rigidity, ductility, and energy dissipation [9]. Fan et al.'s study results showed that RAC works better when combined with ultra-high toughness cementitious composites and fiber-reinforced cementitious materials [10]. Another study on RAC showed that high-strength concrete beams that use CFRP bars can maintain their structural performance when 75% of their concrete is replaced with RAC [11]. RCA material studies show that higher porosity, water absorption, and adhered mortar content lead to lower compressive strength, tensile strength, flexural strength, and elastic modulus, which depend on the replacement ratio [12]. Research has shown that multiple recycling cycles lead to fiber and aggregate property loss, which limits the number of times fiber-reinforced recycled aggregates can be reused [13]. A study of dynamic loading on steel fiber-reinforced RAC showed that fiber orientation, strain rate, and RCA content determine the stress transfer mechanisms, demonstrating that RAC material behaves according to multiple parameters that interact with each other [14].

A number of techniques have been used by researchers to improve RAC, including treatment of RCA with pozzolanic materials, immersion in acidic solutions, mechanical treatment, and thermal treatment [8,15,16]. Various types of fibers have also been added to the mix [17–19]. Some fibers have been found to play an important role in enhancing the ITZ region by acting as bridges between microcracks, thereby increasing the concrete's strength. Other fibers have been used in RAC in an effort to enhance its mechanical properties, such as steel fibers (SFs) [20], basalt fibers (BFs) [17], polypropylene fibers (PPFs) [21], and glass fibers (GFs) [22].

RAC shows better performance in terms of increased strength with the addition of fibers compared to NAC, which can be attributed to its relatively weaker matrix. Another reason is that the bond strength of RAC particles to cement is relatively unstable. Moreover, the inclusion of fibers in concrete helps to reduce the formation of microcracks. Thus, the tensile strength of concrete is improved. Several studies [23] have shown that the inclusion of fibers improves the strength of RAC.

Although using a single type of fiber limits the potential for RAC enhancement, hybrid fibers help overcome this limitation by combining the advantages of each fiber type. Using high-strength and flexible fibers helps create a harmonious combination that has a beneficial effect on the mechanical strength of RAC. At a micro-level, using different types of fiber helps increase connectivity in the calcium silicate hydrate (C-S-H) gel matrix, thus improving the strength and reducing cracks in the concrete matrix [24]. Recent experimental studies have shown that the specific types of fibers and their proportion ratios are the main factors that affect the mechanical properties. For example, the splitting tensile strength and flexural strength were improved by up to 17.5% and 23%, respectively, in the presence of a hybrid system of polypropylene fiber and basalt fiber. The optimum proportion ratios were found to be 6 $kg/m^3$ polypropylene fiber and 6 $kg/m^3$ basalt fiber [25]. In the context of hybrid glass–polypropylene fiber RAC, the test results showed that the proportion ratios of the fibers have a significant effect on the compressive strength and splitting tensile strength. The optimum proportion ratios were found to be 7/3 [26]. In the context of a hybrid system

of recycled steel fiber and textile fiber, the test results showed that the proportion ratios of the fibers have a significant effect on the compressive strength, splitting tensile strength, and flexural strength [27]. In the context of prior studies conducted by Ali [28] and He et al. [29], the test results showed that the compressive strength, splitting tensile strength, and flexural strength were improved by up to 17%, between 14% and 52%, and between 23% and 60%, respectively, from using macro steel fiber and micro polypropylene.

Artificial intelligence (AI) is advancing, and several applications of machine learning (ML) are being developed in civil engineering. These developments are also introducing new ways to approach complex problems and create better predictions than currently possible with regression-based approaches [1]. In practice, ML uses historical data to identify patterns between inputs and desired outcomes. Models like deep neural networks (DNNs) and extreme gradient boosting (XGBoost) can learn from nonlinear relationships between inputs and desired outcomes and continue to provide reasonably accurate predictions as data grows. Reference [30] showed that XGBoost achieved better prediction accuracy than the other boosting models for predicting the mechanical properties of concrete.

These algorithms are used by engineers worldwide to develop models for predicting various engineering parameters [31–33]. Bayesian optimization (BO), particle swarm optimization (PSO), and the bald eagle search algorithm (BES) are examples of optimization techniques frequently used in developing engineering parameter prediction models. Common to all ML techniques is the ability to model complex relationships among many variables within a dataset, which has historically been difficult with traditional regression approaches [34,35].

Numerous studies have examined single fibers or multiple fibers to predict the mechanical properties of RAC [31,36–39]. Although these studies have addressed most fiber types, they remain limited. Very few machine learning models can simultaneously predict compressive, tensile, and flexural strengths for multiple fiber types. They also did not include fiber diameter, length, or volume fraction in their predictions, even though these properties significantly affect the mechanical properties of fiber-reinforced RAC. Hybrid fiber combinations were not considered either. Additionally, while some studies used SHAP analysis to examine the influence of features on mechanical properties, they did not account for interactions among multiple features.

This study aims to improve ML models for predicting the compressive, splitting tensile, and flexural strengths of RAC reinforced with fibers, including hybrid combinations. To accomplish this, 278 sets from 14 peer-reviewed papers were collected [8,17,20–25,29,38,40–43]. Two algorithms were employed—DNN and XGBoost—and hyperparameters were optimized using PSO, BO, and BES. The dataset preparation included imputation, scaling, one-hot encoding, and k-means++ clustering to mitigate potential biases arising from data-split imbalances. A variety of performance criteria were evaluated for the models, and both sensitivity and SHAP analyses were used to assess the individual and coupled effects of fiber characteristics on mechanical properties. This approach allows accurate prediction of RAC properties for multiple fiber types while capturing the influence and interactions of fiber features, guiding efficient mix design and reducing experimental costs.

## 2. Research Significance and Objectives

This study enhances ML-based predictions of fiber-reinforced RAC by facilitating the concurrent estimation of compressive, splitting tensile, and flexural strengths for various single- and hybrid fiber systems while explicitly accounting for fiber geometry, content, and their interactions.

The main aims of this research are as follows:

1. Create ML models to predict compressive, splitting tensile, and flexural strengths of fiber-reinforced RAC.
2. Assemble a comprehensive dataset encompassing various fiber kinds and hybrid combinations.
3. Assess the performance of DNN and XGBoost models.
4. Use particle swarm optimization, Bayesian optimization, and Bayesian ensemble search to optimize hyperparameters for the models.
5. Address data-split-imbalance-related biases via k-means clustering.
6. Interpret the SHAP analysis of fiber properties as both independent and combined factors.

## 3. Modeling Framework and Approach

This section describes the general methodology used to create accurate prediction models for fiber-reinforced RAC. It outlines the data-preparation approach, model construction, validation, and performance-evaluation procedures. Machine learning models are integrated with optimization approaches to improve predictability and robustness. The framework also includes interpretation tools for assessing model dependability and forecast performance.

### *3.1. K-Means++ Algorithm*

The standard k-means algorithm has a significant drawback: its random selection of initial centroids; however, k-means++ addresses this issue by using a more intelligent method. K-means++ randomly selects an initial centroid. Then, after the initial selection, each new centroid is selected based on a probability proportional to the square of the distance to the nearest centroid. K-means++ still follows the same logic as regular k-means: it assigns each sample to the closest centroid, then computes the mean of the points assigned to that centroid, and updates the centroids accordingly. K-means++ reduces randomness in selecting initial centroids and yields more stable clusters, thereby accelerating convergence; however, it requires additional computation during the initialization phase [44]. The k-means clustering algorithm was performed for a value of k = 5. Instead of optimizing k as a hyperparameter, its value was set based on the mechanical heterogeneity observed in fiber-reinforced recycled aggregate concrete. If values lower than k = 5 are used for the k-means clustering algorithm (k = 3), overly general groups are obtained that merge mechanically distinct mixture systems, such as single-fiber and hybrid fiber systems. In such cases, the efficacy of the cluster-based bias control would be reduced. If values larger than k = 5 are used for the k-means clustering algorithm (e.g., k = 6), over-segmentation occurs, and empty clusters are obtained due to insufficient experimental data for certain types of hybrid fiber systems.

### *3.2. K-Fold Cross-Validation*

By splitting the data into k-folds and rotating the folds as the test set, k-fold cross-validation provides reliable estimates of how well the algorithm performs during training. Studies have demonstrated that varying values of "k" produce differences not only in the accuracy of each k-fold model but also in the variance of k-fold model prediction accuracy, bias, and training computational costs. Therefore, there is no one-size-fits-all value of "k" for every machine learning algorithm and dataset. A smaller value of "k" will reduce the computational cost of model training but increase the amount of bias introduced. Conversely, a larger value of "k" requires more computations and increases the variance during model training. For our study, "k" was set to five folds so that we were able to achieve balance when evaluating the performance of both DNNs and XGBs

while maintaining appropriate levels of computational time during the multiple iterations of training the models, as well as ensuring sufficient data to assess the actual performance of each trained model [45]. The flowchart is illustrated in Figure 1.

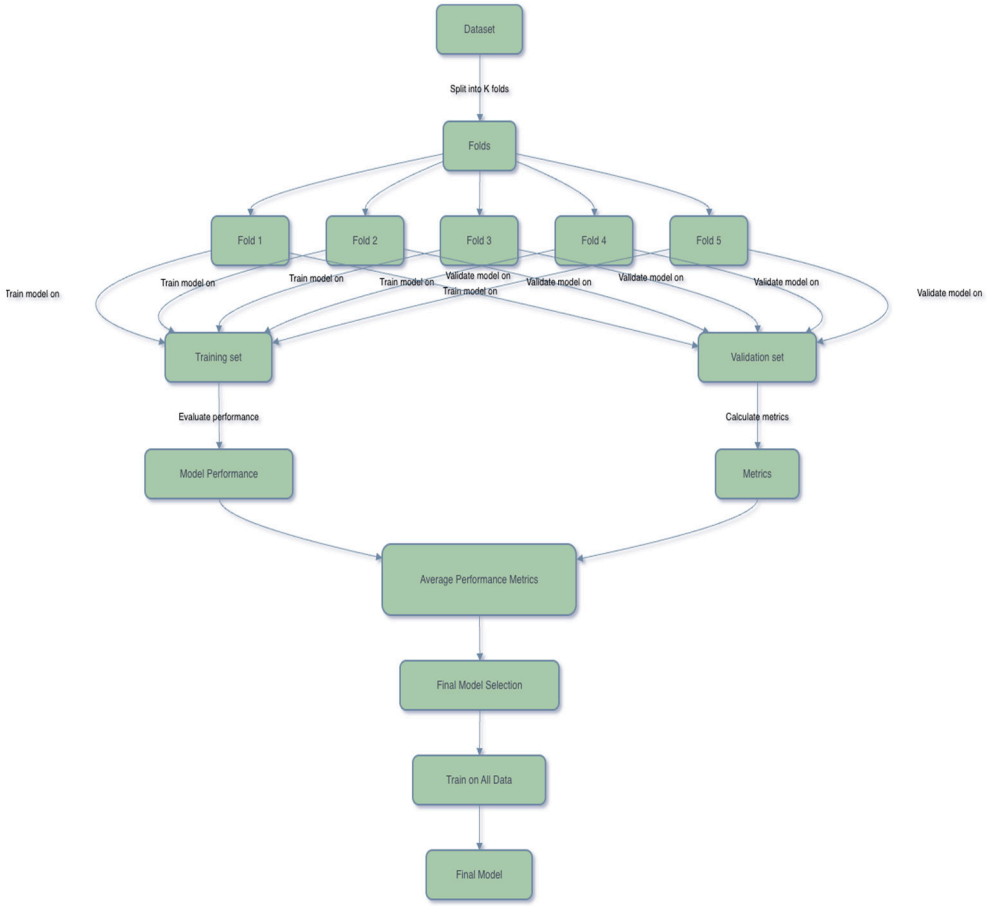


**Figure 1.** Flowchart of k-fold cross-validation.

### *3.3. ML Models*

#### 3.3.1. Deep Neural Network

DNNs are modeled after biological neural networks found in the human brain; this means that, from the DNN perspective, the neurons are the layers that work together to dynamically combine and process information based on their own inputs (i.e., how the neurons connect and interact). A DNN consists of three or more interconnected layers: an input layer, one or more hidden (intermediate processing) layers, and an output layer, which together form a multi-layered perceptron (MLP) architecture (see Figure 2a). Within the MLP architecture, each neuron receives its inputs (weighted inputs), adds a bias term (weighting) to the combination of inputs, and subsequently uses the combined values to produce a result using an appropriate activation function. Several activation functions can be used by a DNN, including the tan-sigmoid function (see Figure 2b) that converts the sum of inputs into a nonlinear output value. The DNN takes a vector of input feature values from the input layer into the hidden layers for processing, learns complex features of the input data, and eventually provides predictions of the associated output vectors from the DNN's output layer. Multiple hidden layers within the architecture enable a DNN to form a pattern of interconnected neurons to represent complex relationships between inputs and outputs, hence the name "multi-layer perceptron." A DNN architecture can be thought of as an advanced version of the traditional single-layer perceptron, which could not model complex input/output relationships; therefore, a DNN is considered to

perform significantly better than a standard single-layer perceptron [36,46]. A feedforward deep neural network was employed in this study using scikit-learn's MLPRegressor. The input layer of the network has as many inputs as there are features in the normalized and one-hot-encoded data. It has a single hidden layer with up to 300 neurons, determined by the optimization procedure, and a single output neuron. In this study, the hidden layer employed the ReLU activation function, whereas the output layer employed linear activation because it was intended for regression.

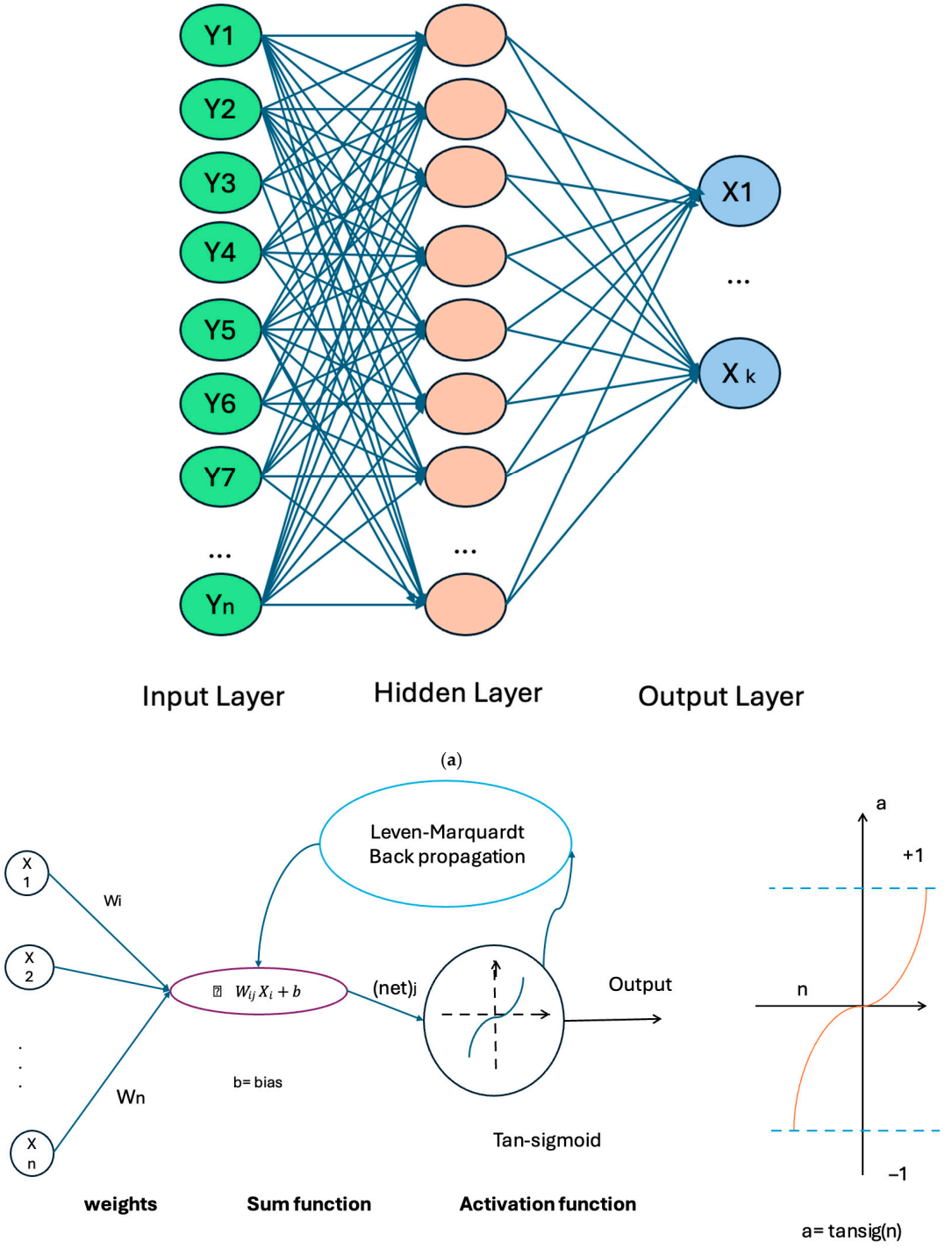


**Figure 2.** Structure and activation mechanisms of a typical DNN: (**a**) one hidden layer architecture, (**b**) hidden and output layer activations and activation functions.

3.3.2. Extreme Gradient Boosting

XGBoost is an ensemble-based gradient-boosting method that improves prediction accuracy by sequentially applying decision trees. Each new tree added after the prior one improves the predictions of the previous trees by correcting the errors they made; therefore, at the end of this process, a strong, highly accurate, and generalizable model is built. XGB can efficiently handle high-dimensional input spaces and control overfitting through a regularization term. Additionally, XGB uses a second-order Taylor series expansion to determine optimal loss functions that allow precise control of the model's hyperparameters and parameters. The objective function for XGB contains two components: the loss function, which measures how well the prediction model performs, and the regularization term, which penalizes too many curves being drawn through the data points. The workflow for generating XGB representations is shown in Figure 3. The process begins with building an individual decision tree and then calculating the residual errors based on the difference between actual and predicted outputs for every observation in the dataset. Additional trees are generated sequentially until convergence conditions are met [47].

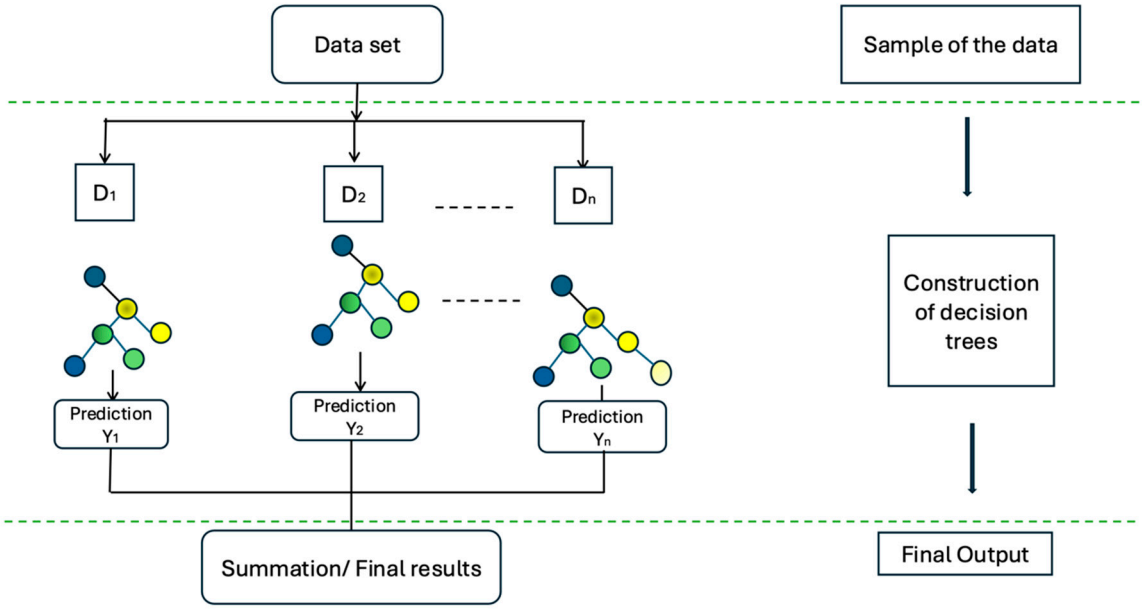


**Figure 3.** Structure of the XGBoost Algorithm.

*3.4. Optimization Methods*

3.4.1. Particle Swarm Optimization (PSO)

The PSO algorithm is a population-based search heuristic inspired by the collective behavior of a school of fish and a flock of birds. This allows the available options to be explored cooperatively. Moreover, the PSO search heuristic allows each particle to modify its velocity by computing an optimal position based on the particle's own best experience and the best experience of the entire population. The movement of the particles is determined by two equations:

$$S_i(\mathrm{t}+1) = \mathrm{w}\cdot S_i(\mathrm{t}) + c_1\cdot r_1\cdot(P_{\mathrm{best,i}} - L_i) + c_2\cdot r_2\cdot(g_{\mathrm{best}} - L_i) \quad (1)$$

$$L_i(\mathrm{t}+1) = L_i(\mathrm{t}) + S_i(\mathrm{t}+1) \quad (2)$$

In these equations, $S_i$(t) is the speed of the ($i$) particle at iteration t, $L_i$ (t) is the current location of that particle, $P_{\mathrm{best,i}}$ is the best location the (i) particle has been able to reach so far, and $g_{\mathrm{best}}$ is the best location that the entire swarm has reached. The inertia weight w is a constant coefficient that controls the influence of the previous velocity on the current

velocity. The acceleration coefficients $c_1$, $c_2$, in conjunction with randomly generated values $r_1$, $r_2$, determine the stochastic movement of each particle toward the optimal solution [48]. PSO in this study was run with w = 0.9, $c_1$ = 0.5, $c_2$ = 0.3, 15 particles, and 10 iterations.

#### 3.4.2. Bayesian Optimization (BO)

BO is a black-box search technique that uses Bayesian reasoning to select the best hyperparameters and is commonly used to optimize hyperparameters in machine learning. BO was shown by [49] to rapidly identify the best-performing hyperparameter combinations for highly complex machine learning models. The BO algorithm uses both a surrogate model and an acquisition function to decide where to explore next. The algorithm uses the acquisition function to identify the most promising location to evaluate in each step. Once an area has been selected, the objective function is evaluated at that location, yielding a new observation ($x_i$, $y_i$). The latest data are incorporated into the current observation set, enabling the surrogate model to be updated before the search resumes. In the present study, BO is used with 25 iterations, five-fold cross-validation, and the $R^2$ scoring metric. The Expected Improvement acquisition function is used by default in the scikit-optimize library.

#### 3.4.3. Bald Eagle Search (BES)

The BES algorithm is based on how bald eagles store their prey, as reported by [50]. The three phases of the BES algorithm represent how the eagle hunts its prey. At first, an eagle selects a promising area for finding food; this location is determined based on a blend of prior knowledge and the eagle's current location and is referred to in the literature as the best-eagle home region. After selecting the best home region, eagles begin to explore this region by following a spiral path around the home location. This spiral motion creates a pattern, thus allowing for more thorough scanning of this region and improving the eagle's scanning ability. The eagle's position is updated using a polar-form formulation, which determines the eagle's current position and uses this position as a base for the next spiral-motion update. Finally, in the final phase of the BES algorithm, eagles swoop towards their prey. A swooping motion updates the eagle's position; by moving it to the best-known location using both the best-eagle home region and the new spiral-based values from the previous phase, an optimal convergence to a solution can be obtained. The three phases of the BES algorithm balance exploration and exploitation, minimizing the risk of the algorithm becoming stuck in a local optimum. In the current study, the BES algorithm is applied with a squad of 15 eagles and 10 iterations. The search radius, R, is controlled by a linearly decreasing scale, which begins at max R = 1.0 and gradually decreases to min R = 0.01. This helps to gradually change the search process from a global to a local approach. The best solution is labeled as the best-eagle home region, where a spiral search is performed, followed by a swoop towards the best eagle. Reproducibility is ensured by fixing the random seed for all runs.

### *3.5. Designed Learning Models for Prediction*

This article presents an integrated ML model for predicting the mechanical properties of fiber-reinforced RAC mixtures using publicly available experimental data. A dataset comprising 278 peer-reviewed compressive strength measurements, 222 splitting tensile strength data, and 195 flexural strength data was used, covering four fiber types: steel, polypropylene, basalt, and glass. There were 19 input parameters: cement ($kg/m^3$), water ($kg/m^3$), fine aggregate ($kg/m^3$), coarse aggregate ($kg/m^3$), recycled aggregate ($kg/m^3$), nanosilica ($kg/m^3$), fly ash ($kg/m^3$), silica fume ($kg/m^3$), GGBS ($kg/m^3$), superplasticizer (%), fiber volume fraction (%), average fiber length (mm), fiber diameter (mm), hybrid fiber volume fraction (%), average hybrid fiber length (mm), hybrid fiber diameter (mm),

and curing age (days). The output targeted the compressive, splitting tensile, and flexural strengths of RAC. The feature statistics are summarized in Table 1.

**Table 1.** Feature set data.

| Feature Parameter | Average | Minimum | Maximum | Standard Deviation | Kurtosis | Skewness |
|---|---|---|---|---|---|---|
| Cement (kg/m$^3$) | 406.4 | 225 | 540 | 71.99 | 0.90 | −0.57 |
| Water (kg/m$^3$) | 207.75 | 170 | 343.5 | 33.11 | 9.80 | 2.93 |
| Fine Aggregate (kg/m$^3$) | 693.22 | 548 | 942 | 113.07 | −0.99 | 0.38 |
| Coarse Aggregate (kg/m$^3$) | 429.75 | 0 | 1210 | 451.15 | −1.35 | 0.45 |
| Recycled Aggregate (kg/m$^3$) | 589.76 | 0 | 1210 | 432.14 | −1.49 | −0.24 |
| Nanosilica (kg/m$^3$) | 3.13 | 0 | 34 | 8.7 | 6.02 | 2.71 |
| Fly Ash (kg/m$^3$) | 30.7 | 0 | 164 | 52.33 | 0.4 | 1.38 |
| Silica Fume (kg/m$^3$) | 4.96 | 0 | 44 | 12.78 | 4.16 | 2.39 |
| GGBS (kg/m$^3$) | 18.59 | 0 | 250 | 62.31 | 9.67 | 3.36 |
| Superplasticizer (%) | 0.63 | 0 | 2 | 0.68 | −0.33 | 0.91 |
| Fiber Volume Fraction (%) | 0.62 | 0.04 | 1.8 | 0.51 | −0.96 | 0.55 |
| Average Fiber Length (mm) | 21.04 | 6 | 50 | 11.44 | −1.13 | 0.27 |
| Fiber Diameter (mm) | 1.1 | 0.01 | 16 | 3.4 | 15.03 | 4.03 |
| Hybrid Fiber Volume Fraction (%) | 0.52 | 0.1 | 1.5 | 0.41 | −0.24 | 0.77 |
| Average Hybrid Fiber Length (mm) | 22.63 | 6 | 50 | 16.42 | −1.11 | 0.79 |
| Hybrid Fiber Diameter (mm) | 0.24 | 0.02 | 0.75 | 0.29 | −1.07 | 0.83 |
| Curing Age (days) | 26.95 | 3 | 90 | 17.09 | 5.94 | 1.98 |
| Compressive Strength (MPa) | 38.79 | 14.77 | 73.11 | 12.17 | −0.51 | 0.3 |
| Splitting Tensile Strength (MPa) | 2.92 | 1.43 | 6.6 | 0.92 | 0.28 | 0.66 |
| Flexural Strength (MPa) | 4.17 | 1.48 | 9.3 | 1.76 | −0.02 | 0.63 |

The research methodology is illustrated in Figure 4 and encompasses the workflow from data collection through evaluation and deployment of the predictive models. After acquiring the necessary data, the dataset was pre-processed: missing values were handled, and numerical features were scaled using a unified transformation pipeline that included one-hot encoding for categorical features. A clustering strategy based on the k-means++ algorithm was applied to the complete dataset to produce balanced training and test sets and to mitigate sampling bias during training. Two predictive models were used to generate the final outputs: a DNN and an XGBoost model. For DNN models, the network configuration and learning parameters were also determined using the same optimization process as that used for the XGBoost models. The number of neurons in the hidden layer of DNN models was treated as an optimization parameter and searched over the range 50–300. The learning rate was optimized over the range of $10^{-4}$ to $10^{-1}$, while the L2 regularization parameter (alpha) was included to avoid overfitting. The DNN models were trained for a maximum of 800 iterations, and the final configuration was determined based on five-fold cross-validation $R^2$ scores for each target property. This process provided transparency in selecting the best. There are six combinations in total. These combinations include DNN-BO, DNN-PSO, DNN-BES, XGB-BO, XGB-PSO, and XGB-BES. The hyperparameters of a model are determined by probing its hyperparameter space using a probabilistic search method, such as BO. PSO relies on how particles move along a route, while the bald eagle search (BES) uses the hunting behavior of bald eagles to fine-tune the model's parameter combinations. All models use five-fold cross-validation to assess their accuracy.

The accuracy of each model was evaluated using six metrics ($R^2$, RMSE, MAE, MAPE, SMAPE, U95), and the best model for each target property was selected based on all six metrics. The best model, as determined by the metrics, was studied using a Shapley interaction analysis to understand the contributions of variables and their impacts on the

mechanical performance of the fiber-reinforced concrete by identifying the overall influence of mixture proportions, fiber geometry, and hybrid interactions on the performance of the model.

The trained models are available to the public via an interactive web-based interface built with Hugging Face Spaces and Gradio. The interface allows users to enter mixed proportions and receive predictions immediately. This tool will be beneficial to both practitioners and the research community.

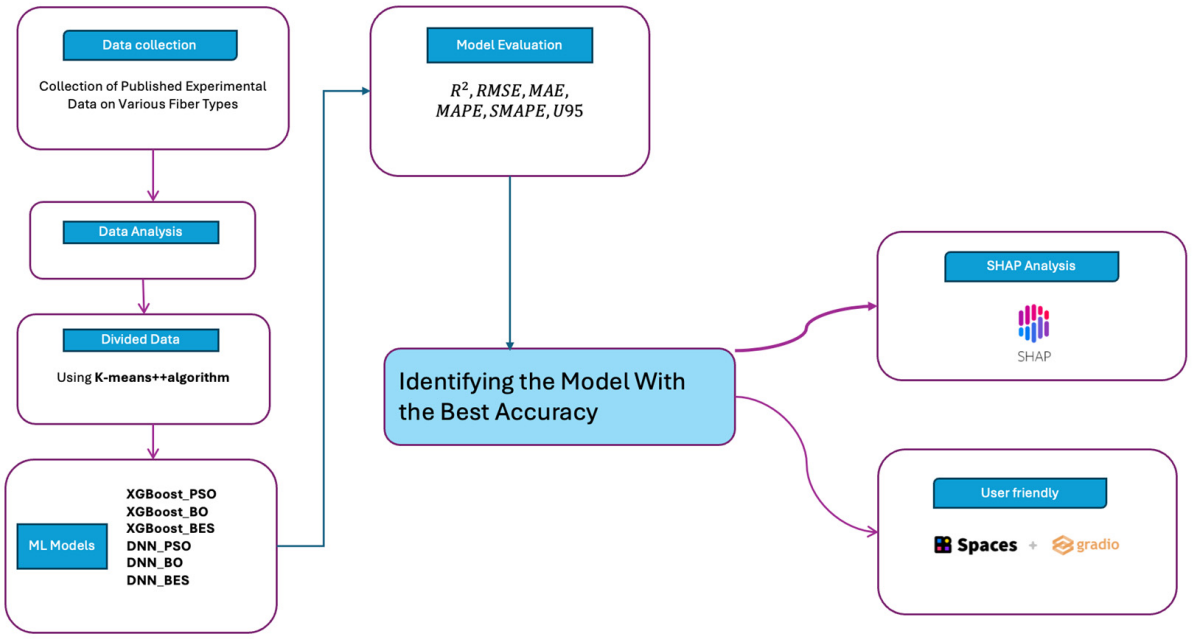


**Figure 4.** Overview of the proposed framework.

### *3.6. Evaluation Indicators*

For this research, six metrics were used to measure the model's prediction performance. They are $R^2$ (which indicates how much variation in the target variable is accounted for by the model), mean absolute percentage error (MAPE), symmetric MAPE (SMAPE), mean absolute error (MAE), root mean squared error (RMSE), and 95% uncertainty interval (U95).

$$\mathrm{R}^2 = 1 - \frac{\sum_{i=1}^{s}(y_\mathrm{i} - \hat{y}_\mathrm{i})^2}{\sum_{i-1}^{s}(y_\mathrm{i} - y)^2} \tag{3}$$

$$\mathrm{RMSE} = \sqrt{\frac{1}{s}\sum_{i=1}^{s}(y_\mathrm{i} - \hat{y}_\mathrm{i})^2} \tag{4}$$

$$\mathrm{MAE} = (1/\mathrm{s})\sum_{i=1}^{s}|y_\mathrm{i} - \hat{y}_\mathrm{i}| \tag{5}$$

$$\mathrm{MAPE} = \frac{1}{s}\sum_{i=1}^{s}\frac{y_\mathrm{i} - \hat{y}_\mathrm{i}}{y_\mathrm{i}} \tag{6}$$

$$\mathrm{SMAP} = \frac{100}{s}\sum_{i=1}^{s}\frac{|y_\mathrm{i} - \hat{y}_\mathrm{i}|}{\frac{|y_\mathrm{i}| - |\hat{y}_\mathrm{i}|}{2}} \tag{7}$$

$$\mathrm{U95} = 1.96\sqrt{SD^2 + RMSE^2} \tag{8}$$

where $y_\mathrm{i}$ is the observed output, $\hat{y}_\mathrm{i}$ is the predicted output, $y$ is the mean of observed values, $s$ is the number of tasters, and the standard deviation of the errors is SD. R2 indicates how well the model can clarify a proportion of the variance within the target variable; a zero value indicates no explanatory power, and a value of 1 indicates a perfect

fit. In other words, higher values would demonstrate much stronger model fits. MAE and RMSE measure the average prediction error in the same units as the target variable. MAPE gives an average percentage error, allowing direct comparison of results, with each metric dimensionless. However, unlike MAPE, which accounts for all errors by measuring absolute values only, SMAPE estimates the amount of over- or under-prediction; hence, both types are expressed as percentages. Finally, U95 defines the prediction uncertainty as the difference between the average prediction and the 95% confidence interval. Collectively, they provide a comprehensive overview of the model's accuracy, reliability, and consistency in predicting compressive strength [51,52].

## 4. Results and Discussion

### *4.1. Model Predictions and Performance Comparison*

Several metrics were used to evaluate the models' predictive performance across both the training and testing datasets (Table 2), including $R^2$, RMSE, MAE, MAPE, SMAPE, and U95. The residual plots and error histograms provided a visual representation of the models' predictions and an evaluation of their trustworthiness.

**Table 2.** Model evaluation on training and test data.

| Target | Model | Opt | R2 | | RMSE | | MAE | | MAPE | | SMAPE | | U95 | |
|---|---|---|---|---|---|---|---|---|---|---|---|---|---|---|
| | | | Train | Test | Train | Test | Train | Test | Train | Test | Train | Test | Train | Test |
| Compressive strength | DNN | BO | 0.846 | 0.795 | 4.696 | 5.792 | 3.447 | 4.365 | 10.370 | 11.768 | 9.625 | 11.163 | 12.457 | 15.754 |
| | | PSO | 0.797 | 0.759 | 5.391 | 6.280 | 4.244 | 4.983 | 11.677 | 12.768 | 11.858 | 13.048 | 14.692 | 17.161 |
| | | BES | 0.824 | 0.805 | 5.015 | 5.647 | 3.988 | 4.381 | 10.776 | 11.448 | 11.192 | 11.822 | 13.393 | 15.313 |
| | XGB | BO | 1.000 | 0.949 | 0.037 | 2.893 | 0.025 | 1.817 | 0.074 | 4.356 | 0.074 | 4.460 | 0.102 | 7.974 |
| | | PSO | 0.997 | 0.972 | 0.612 | 2.158 | 0.438 | 1.507 | 1.216 | 4.036 | 1.213 | 4.176 | 1.697 | 5.919 |
| | | BES | 0.996 | 0.968 | 0.772 | 2.303 | 0.571 | 1.728 | 1.575 | 4.463 | 1.571 | 4.546 | 2.140 | 6.355 |
| Splitting tensile strength | DNN | BO | 0.962 | 0.745 | 0.183 | 0.428 | 0.131 | 0.284 | 4.959 | 9.139 | 4.908 | 9.342 | 0.506 | 1.186 |
| | | PSO | 0.950 | 0.753 | 0.208 | 0.421 | 0.155 | 0.294 | 5.763 | 9.432 | 5.701 | 9.602 | 0.576 | 1.166 |
| | | BES | 0.959 | 0.784 | 0.190 | 0.393 | 0.135 | 0.267 | 4.801 | 8.595 | 4.834 | 8.869 | 0.516 | 1.082 |
| | XGB | BO | 1.000 | 0.858 | 0.005 | 0.320 | 0.003 | 0.228 | 0.144 | 7.032 | 0.144 | 7.255 | 0.013 | 0.881 |
| | | PSO | 0.999 | 0.899 | 0.028 | 0.269 | 0.020 | 0.193 | 0.811 | 5.972 | 0.810 | 6.013 | 0.077 | 0.746 |
| | | BES | 0.999 | 0.888 | 0.022 | 0.284 | 0.016 | 0.203 | 0.683 | 6.254 | 0.683 | 6.314 | 0.062 | 0.787 |
| Flexural strength | DNN | BO | 0.984 | 0.800 | 0.226 | 0.772 | 0.168 | 0.454 | 4.713 | 10.169 | 4.667 | 10.064 | 0.626 | 2.129 |
| | | PSO | 0.981 | 0.823 | 0.241 | 0.727 | 0.176 | 0.437 | 4.872 | 9.523 | 4.837 | 9.285 | 0.667 | 1.998 |
| | | BES | 0.979 | 0.835 | 0.252 | 0.702 | 0.188 | 0.437 | 5.312 | 10.330 | 5.201 | 9.720 | 0.690 | 1.893 |
| | XGB | BO | 1.000 | 0.874 | 0.035 | 0.612 | 0.024 | 0.270 | 0.767 | 6.064 | 0.767 | 6.188 | 0.097 | 1.696 |
| | | PSO | 0.999 | 0.898 | 0.048 | 0.553 | 0.030 | 0.269 | 1.011 | 6.459 | 1.012 | 6.725 | 0.132 | 1.525 |
| | | BES | 0.999 | 0.905 | 0.044 | 0.533 | 0.029 | 0.280 | 0.983 | 6.609 | 0.984 | 6.860 | 0.122 | 1.471 |

Across the training datasets, XGBoost models produced highly accurate predictions for compressive, splitting tensile, and flexural strengths. The $R^2$ values were between 0.99 and 1.00; for RMSE values, they were less than 0.772 MPa; for MAE, the maximum values were less than 0.571 MPa. The maximum values for MAPE and SMAPE were less than 1.575%, while the maximum U95 values were less than 2.14 MPa. The DNN models achieved moderate to high accuracy for compressive, splitting tensile, and flexural strengths. The $R^2$ values ranged from 0.797 to 0.984. The RMSE values ranged from 0.183 to 5.391 MPa, and the MAE ranged from 0.131 to 4.244 MPa, both demonstrating

acceptable average prediction errors. All the training set's MAPE values were less than 11.677 percent; consequently, all of the SMAPE values were less than 11.858 percent. U95 predictive intervals ranged from 0.506 to 14.692 MPa, indicating moderate uncertainty in the target variable, depending on which training data point was selected.

DNN models on the testing datasets exhibited a significantly larger genuine prediction error across all target property datasets than XGBoost models did. The test $R^2$ values for the DNNs were consistently above 0.75 but were always much lower than those for XGBoost, which reached 0.86. RMSE, MAE, MAPE, and SMAPE errors for DNNs were also greater than those for XGBoost, with RMSE and MAE of 6.28 MPa and 4.98 MPa, respectively; however, XGBoost had substantially lower errors than DNNs across all other metrics. The U95 values were also higher for DNNs than for XGBoost, indicating that DNN generalization was inferior to XGBoost generalization.

The best-performing model, BO-XGBoost, on the training datasets achieved $R^2$ values greater than 0.99 and an RMSE of approximately 0.037 MPa.

PSO-XGBoost was the top-performing model on the test set for compressive strength and splitting tensile prediction, achieving the highest $R^2$ (0.972, 0.899), respectively, and the lowest RMSE and MAE among the other models tested. For flexural strength prediction, BES-XGBoost achieved the best performance and was very close to PSO-XGBoost and BO-XGBoost. Figure 5 shows the models' performance in predicting compressive strength on the training and testing datasets. In the training dataset, most data points cluster near the 45° line, supporting the conclusion that the model captures a strong relationship between the input and output variables. This indicates that very few of the prediction points are substantially separated from the diagonal, suggesting strong correlation across almost all predicted strength values in the training dataset. The same basic trend was observed in the test set, but the number of predicted points deviating from the diagonal line increased. However, the distribution of points remains clearly concentrated along the diagonal, and most predictions remain close to their actual values. Although there are only a few significant divergences from model predictions on the unseen test set, the models' performance on this set suggests high generalizability across the entire dataset.

The error distribution histograms were analyzed to assess predictive accuracy for the models further (Figure 6). The DNN models with optimization had a much broader range of errors, with many predictions falling out of the range of $\pm$10 MPa for compressive strength, $\pm$0.5 MPa for splitting tensile strength, and $\pm$1 MPa for flexural strength. Therefore, these models did not identify all appropriate characteristics for every sample and, consequently, exhibited the lowest predictive accuracy.

However, the BES-XGBoost, PSO-XGBoost, and BO-XGBoost models exhibited a much more concentrated error range. The errors for compressive strength were within $\pm$2 MPa, while those for splitting tensile and flexural strength were within $\pm$0.2 MPa and $\pm$0.5 MPa, respectively. Among these models, the PSO-XGBoost exhibited the most concentrated error distribution, thereby demonstrating the highest accuracy, generalization, and stability.

The low U95 value for the PSO-XGBoost model further supports this conclusion, indicating that predicted concrete strengths with fiber had minimal variation. The reproduction test showed that the model performed consistently across all partitions, with minor differences in error standard deviation. This indicates that the PSO-XGBoost model is robust across changing datasets.

Overall, the XGBoost model proved to be the most reliable and accurate for predicting concrete mechanical properties, combining high training precision, excellent generalizability, and minimal uncertainty in predictions.

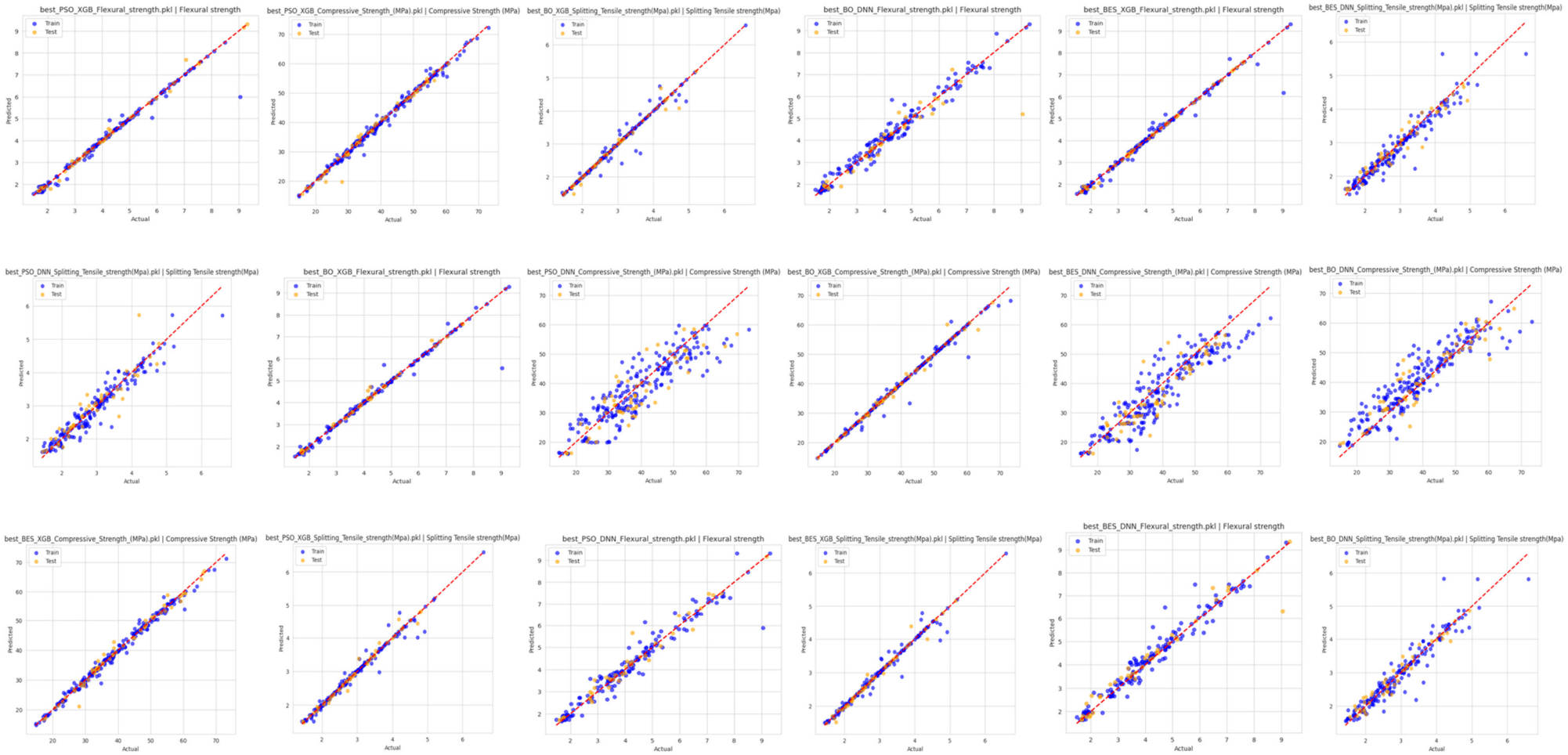


**Figure 5.** Performance of regression models.

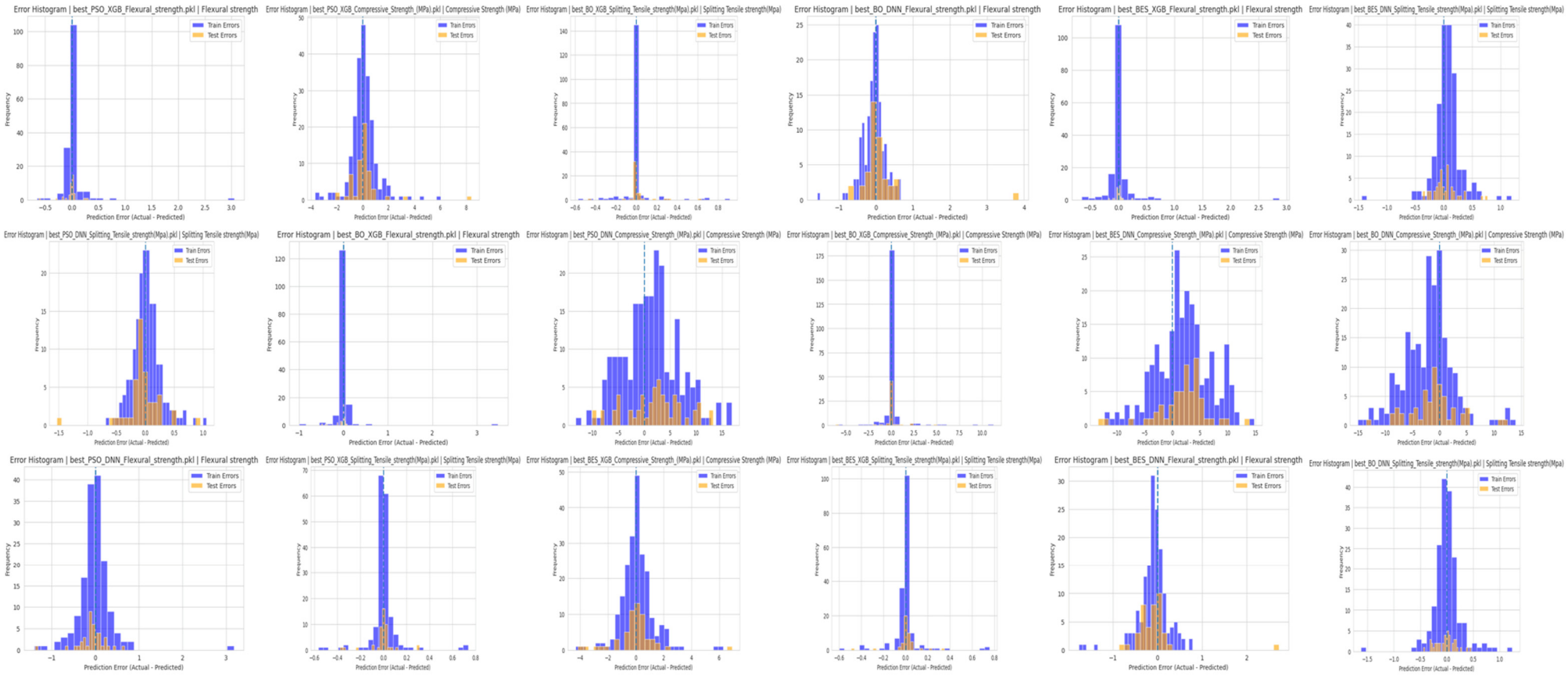


**Figure 6.** Error analysis histogram.

### 4.2. Understanding Feature Influence Through SHAP

To determine how the individual input features of fiber-reinforced concrete affect its mechanical properties, sensitivity analyses were performed on the optimal models using SHAP (SHapley Additive exPlanations). SHAP provides a post-reconstruction explanation of model outputs by quantifying the contribution of each input feature to each prediction, and it enables global and local interpretation of the model, since there is no need to interpret the output using a functional form, as with a black-box model. For each prediction sample, SHAP computes a feature value for each feature that indicates the feature's impact on that model prediction. Based on the results shown in Figure 7a, PSO-XGBoost was the best model for predicting compressive strength. Based on the SHAP results, the two most impactful features were curing age and silica fume percentage, relative to the other features. While fiber type also affects compressive strength, its effect is complex and varies with the specific fiber type, producing both positive and negative impacts on predicted compressive strength. In general, RCA, water content, and fiber diameter show a clear trend: as fiber diameter increases, the predicted compressive strength decreases.

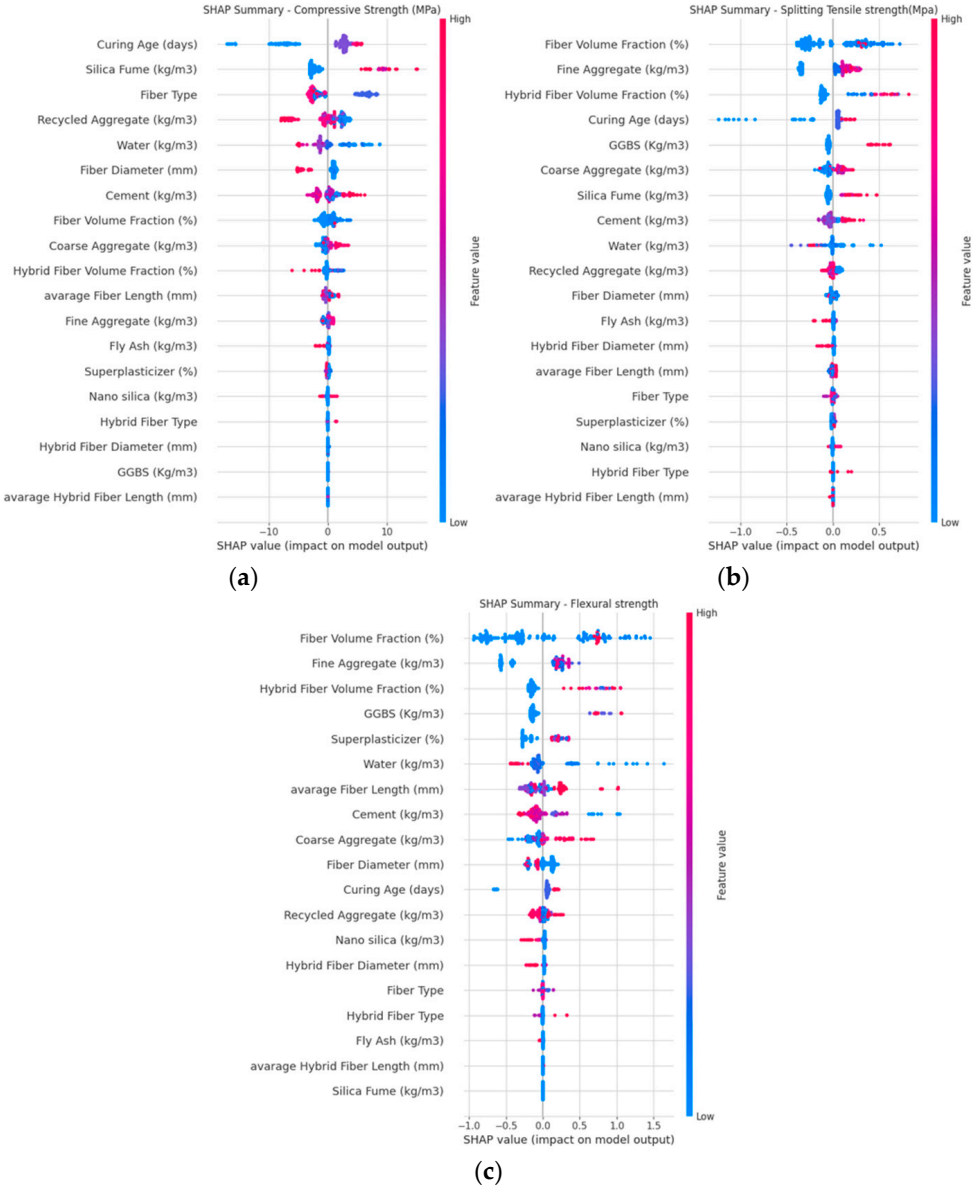


**Figure 7.** SHAP feature: (**a**) PSO-XGBoost compressive strength, (**b**) PSO-XGBoost splitting tensile, (**c**) BES-XGBoost flexural strength.

The splitting tensile strength was best predicted by PSO-XGBoost (Figure 7b). Fiber volume fraction (%) was the most influential predictor of splitting tensile strength; higher fiber volume fraction (%) was associated with greater predicted splitting tensile strength. The hybrid fiber volume fraction (%) also had a substantial positive effect on the prediction of splitting tensile strength, providing further evidence that total fiber content is critical for splitting tensile strength performance. The fine aggregate content was the second most influential factor; higher percentages of fine aggregate improved particle packing and fiber dispersion, thereby enhancing the composite's tensile performance. GGBS also improved tensile strength predictions for the composites by refining the pore structure and strengthening the interfacial transition zone (ITZ) between the fibers and the cement matrix. Conversely, a higher percentage of coarse aggregate adversely affected predictions for the composites, likely due to interference with fiber distribution and the development of localized concentrated stresses.

For predicting flexural strength, BES-XGBoost produced the best predictions (Figure 7c). Fiber volume fraction (%) was once again the dominant factor in the SHAP analysis, with larger volumes strongly associated with increased predicted flexural strength. The hybrid fiber volume fraction (%) and average fiber length (mm) were also significant contributors, underscoring the importance of both the fiber count and the effective fiber length in resisting bending stress. Fiber diameter (mm) had a generally adverse effect on the predictions, indicating that finer fibers are beneficial for bonding between the fiber and matrix. Flexural strength benefited from a higher fine aggregate content, owing to improved packing and matrix homogeneity. A superplasticizer, on the other hand, had a strong positive effect on the flexural strength properties by improving workability and fiber distribution. Conversely, both water content and coarse aggregate adversely affected flexural strength predictions by introducing excess porosity at extreme water content or by reducing tensile strength due to the presence of large aggregate.

Figure 8 shows the results of the interaction analysis based on the SHAP method, which revealed that the influence of the curing age is stronger at higher levels of silica fume and nanosilica content, which is related to long-term hydration and densification of the hydrating gel. The interaction between fiber volume fraction and fiber length suggests that moderate fiber content with higher fiber length improves the strength, while excessive fiber content causes variations. The interaction between fiber volume fraction and fiber diameter indicates that an increased volume fraction of fibers improves strength when smaller diameters are used. However, increased diameter reduces efficiency at higher volume fractions due to bonding efficiency. Considering hybrid fiber volume fraction and hybrid fiber length, moderate volume fractions of fibers along with increased fiber length produce positive contributions, whereas increased volume fractions lead to unstable effects due to dispersion and workability problems. The interaction between fine aggregate content and fiber volume indicates that moderate fine aggregate content enhances the interaction effect of fibers, whereas an increased amount of fines reduces the interaction effect. These results further support the notion that the compressive strength is related to the interaction of material properties rather than their individual effects.

In conclusion, the SHAP analysis quantified the primary driving factors of flexural and tensile performance as those pertinent to the fiber in a hybrid fiber-reinforced concrete while providing vital information regarding curing, silica fume, and aggregate characteristics that govern the compressive strength of fiber-reinforced concrete.

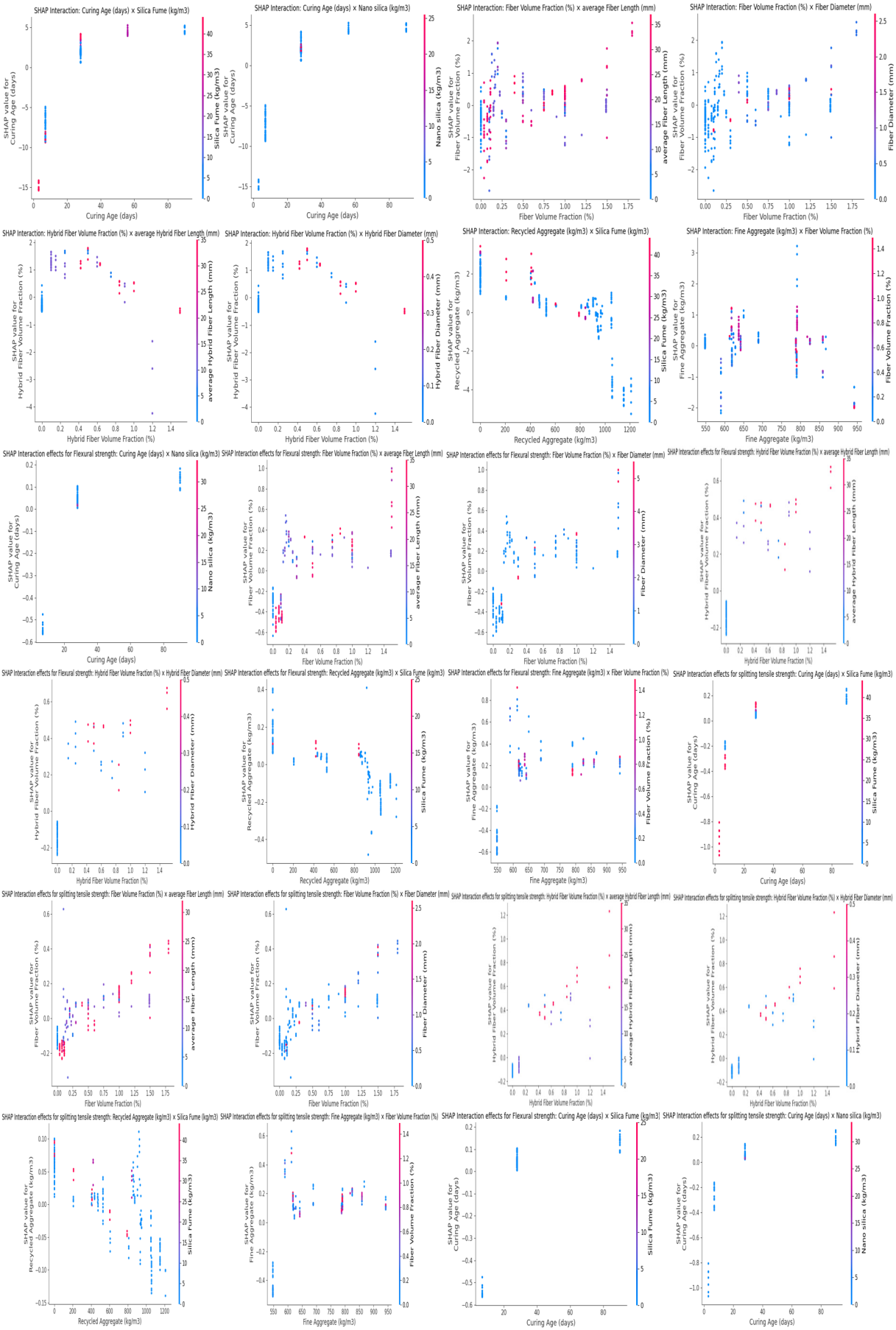


**Figure 8.** SHAP interaction analysis of material parameters.

### 4.3. User-Friendly FRC Mechanical Properties Predictor

Machine learning models were created to provide data to individuals who would likely utilize the solutions in their day-to-day operations. Therefore, the application has been made open-source, allowing anyone to use the tools by visiting the website for the software known as "FRC Strength Predictor," which can be found on Hugging Face Spaces (link available at Insert link: https://huggingface.co/spaces/marwahtik/frc_strength_predictor (accessed on 1 March 2026)).

The "FRC Strength Predictor" is a web-based service that enables engineers and researchers to perform real-time, on-demand calculations of compressive strength, splitting tensile strength, and flexural strength based on the mix design parameters they enter into the application. By transforming the predictive model into a dynamic design tool, the end user can modify input variables, such as fiber volume and water content, and observe the corresponding change in the composite's anticipated strength. This feature will enable improved determination of the optimal proportions of an FRC mix and demonstrate how the model is responsive to the materials used to produce the composite by providing a highly transparent means of visualizing how such alterations will affect the model. Figure 9 shows a screenshot of the developed tool interface.

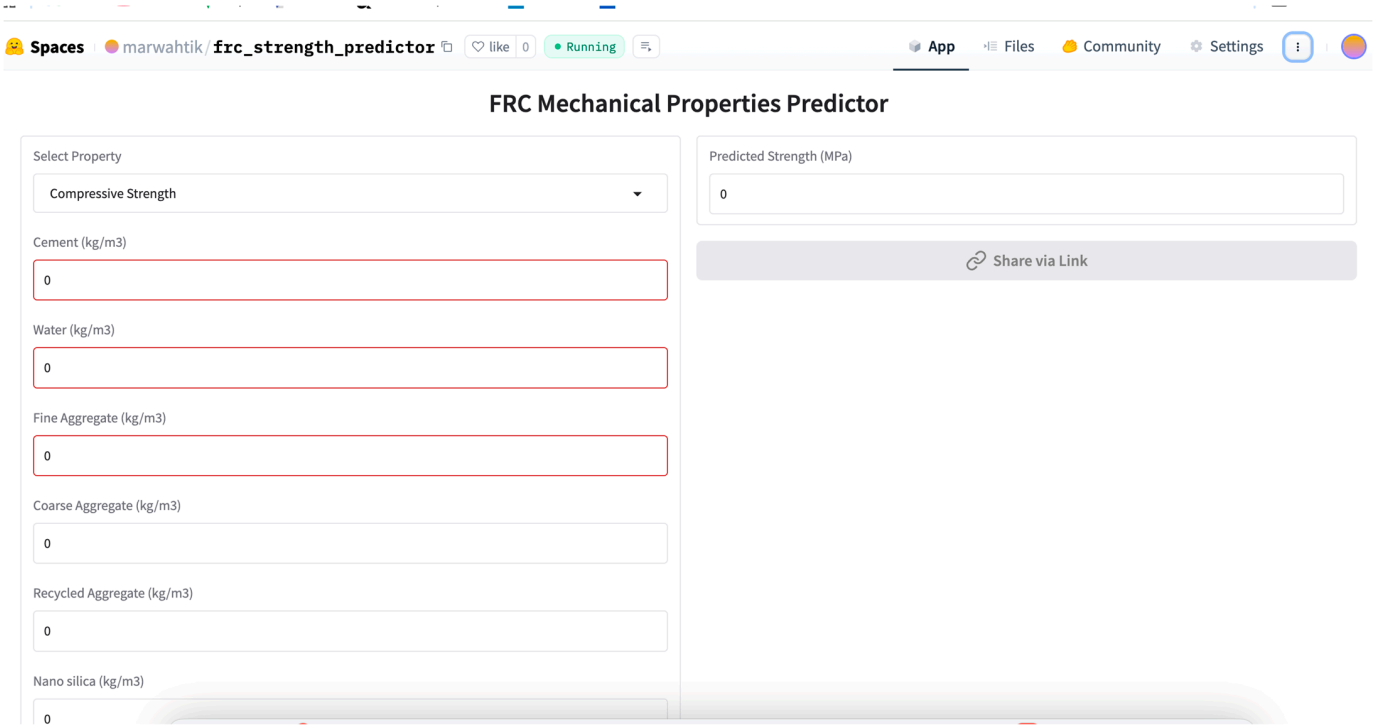


**Figure 9.** FRC prediction tool.

## 5. Conclusions

A new hybrid methodology integrating machine learning and optimization techniques (specifically PSO, BO, and BES) has been developed to build an accurate predictive model for several types of fiber-reinforced concrete containing RCA. The dataset used comprised 278 published compressive strength measurements, 222 splitting tensile strength measurements, and 195 flexural strength measurements from peer-reviewed studies. The k-means++ clustering approach was used to generate a balanced, highly connected testing and training dataset. The six ML models were created by building deep neural networks and XGBoost models and then optimizing each model using BO, PSO, and BES. The final model's accuracy was assessed using R2, MAE, RMSE, SMAPE, MAPE, and U95. The highest-

performing model was also analyzed using SHAP-based sensitivity analysis. Significant findings are listed below:

1. The PSO-XGBoost regressor achieved the highest accuracy in predicting compressive strength. Its training and test sets had the following performance results: R2 (0.997, 0.972), SMAPE (1.213%, 4.176%), RMSE (0.612, 2.158), MAPE (1.216%, 4.036%), U95 (1.697, 5.919), and MAE (0.438, 1.507). As for the splitting tensile strength prediction, the PSO-XG Boost model also captured the most accurate results in the test by capturing the primary mechanism of reinforcement, $R^2$ = (0.899), MAPE (5.972%), U95 (0.746), SMAPE (6.013%), RMSE (0.269), and MAE (0.193). Finally, the BES-XG Boost model achieved the highest accuracy in predicting flexural strength, with a test R2 of 0.905.
2. The two most significant drivers of compressive strength are curing age and the use of silica fume, indicating that the densification and curing of the cement matrix are the primary determinants of compressive strength. With respect to splitting tensile strength and flexural strength, fiber volume fraction and other fiber characteristics are the principal contributors to these properties. This is consistent with the current understanding of flexural strength and splitting tensile strength and with the view that these two properties are driven by the "crack-bridging" mechanism and the material's ability to resist cracking under tension.
3. The SHAP analysis and the user-friendly interface provide engineers with actionable information to optimize concrete mixtures, enabling them to adjust component quantities based on their behavior. For example, if an engineer wants to increase the splitting tensile strength of concrete, they could optimize the fiber content or improve the superplasticizer dosage. Alternatively, if an engineer seeks to optimize the fine aggregate used in a concrete mixture for optimal splitting tensile strength performance, they could examine the SHAP analysis results and the user-friendly interface to identify the optimal amount of fine aggregate.

**Author Contributions:** Conceptualization, M.A.t.; methodology, M.A.t.; software, M.A.t. and A.B.-J.; validation, M.A.t.; formal analysis, M.A.t.; investigation, M.A.t.; resources, M.A.t.; data curation, M.A.t.; writing—original draft preparation, M.A.t.; writing—review and editing, M.A.t., A.B.-J., S.R. and Z.T.; visualization, M.A.t. All authors have read and agreed to the published version of the manuscript.

**Funding:** This research received no external funding.

**Data Availability Statement:** The data presented in this study are available on request from the corresponding author.

**Conflicts of Interest:** The authors declare no conflicts of interest.

## References

1. Bahadori-Jahromi, A.; Room, S.; Paknahad, C.; Altekreeti, M.; Tariq, Z.; Tahayori, H. The role of Artificial Intelligence and Machine Learning in advancing civil engineering: A comprehensive review. *Appl. Sci.* **2025**, *15*, 10499. [CrossRef]
2. Gonzalez-Corominas, A.; Etxeberria, M. Effects of using recycled concrete aggregates on the shrinkage of high performance concrete. *Constr. Build. Mater.* **2016**, *115*, 32–41. [CrossRef]
3. Adams, M.P.; Fu, T.; Cabrera, A.G.; Morales, M.; Ideker, J.H.; Isgor, O.B. Cracking susceptibility of concrete made with coarse recycled concrete aggregates. *Constr. Build. Mater.* **2016**, *102*, 802–810. [CrossRef]
4. Bahraq, A.A.; Jose, J.; Shameem, M.; Maslehuddin, M. A review on treatment techniques to improve the durability of recycled aggregate concrete: Enhancement mechanisms, performance and cost analysis. *J. Build. Eng.* **2022**, *55*, 104713. [CrossRef]
5. Xiao, J.; Li, W.; Fan, Y.; Huang, X. An overview of study on recycled aggregate concrete in China (1996–2011). *Constr. Build. Mater.* **2012**, *31*, 364–383. [CrossRef]

6. Yang, Y. Influence of Recycled Aggregate Strengthen and Adding Fiber on the Properties of Recycled Aggregate Concrete. Doctoral Dissertation, Beijing Jiaotong University, Beijing, China, 2014.
7. Liang, C.; You, J.; Gu, F.; Gao, Y.; Yang, G.; He, Z.; Hou, S.; Duan, Z. Enhancing the elastic modulus of concrete prepared with recycled coarse aggregates of different quality by chemical modifications. *Constr. Build. Mater.* **2022**, *360*, 129590. [CrossRef]
8. Wang, Y.; Hughes, P.; Niu, H.; Fan, Y. A new method to improve the properties of recycled aggregate concrete: Composite addition of basalt fiber and nano-silica. *J. Clean. Prod.* **2019**, *236*, 117602. [CrossRef]
9. Özkılıç, Y.O.; Althaqafi, E.; Karalar, M.; Aksoylu, C. Shear and flexural performance of reinforced concrete beams with recycled concrete aggregates. *Rev. Adv. Mater. Sci.* **2025**, *64*, 20250140. [CrossRef]
10. Fan, X.; Liu, S.; Wei, D.; Gu, Z.; Li, Z. Study on the shear performance of R-UHTCC reinforced recycled concrete composite beams. *Structures* **2025**, *81*, 110219. [CrossRef]
11. Saadi, G.M.S.; Rasheed, M.H.F.; Agha, A.Z.S. Experimental Investigation of CFRP High-Strength Concrete Beams Incorporating Recycled Concrete Aggregate. *Buildings* **2025**, *15*, 1418. [CrossRef]
12. Junior, G.A.; Leite, J.C.; Mendez, G.d.P.; Haddad, A.N.; Silva, J.A.; da Costa, B.B. A review of the characteristics of recycled aggregates and the mechanical properties of concrete produced by replacing natural coarse aggregates with recycled ones—Fostering resilient and sustainable infrastructures. *Infrastructures* **2025**, *10*, 213. [CrossRef]
13. Kovacs, R.; Shamass, R.; Limbachiya, V. Multi-recycling of different concrete products: Effects on recycled aggregate's physical characteristics and compressive strength. *J. Build. Eng.* **2025**, *113*, 114004. [CrossRef]
14. Zhang, X.; Li, Y.; Fan, Y.; Zhou, G.; Huang, Y.; Xu, P.; Ding, Y. Analysis on the impact resistance of steel fiber reinforced recycled aggregate concrete. *Structures* **2025**, *75*, 108599. [CrossRef]
15. Siletani, A.H.; Asayesh, S.; Shirzadi Javid, A.A.; Habibnejad Korayem, A.; Ghanbari, M.A. Influence of coating recycled aggregate surface with different pozzolanic slurries on mechanical performance, durability, and micro-structure properties of recycled aggregate concrete. *J. Build. Eng.* **2024**, *83*, 108457. [CrossRef]
16. Verma, A.; Babu, V.S.; Arunachalam, S. Influence of acetic acid soaking and mechanical grinding treatment on the properties of treated recycled aggregate concrete. *J. Mater. Cycles Waste Manag.* **2022**, *24*, 877–899. [CrossRef]
17. Katkhuda, H.; Shatarat, N. Improving the mechanical properties of recycled concrete aggregate using chopped basalt fibers and acid treatment. *Constr. Build. Mater.* **2017**, *140*, 328–335. [CrossRef]
18. Ahmed, T.W.; Ali, A.A.M.; Zidan, R.S. Properties of high strength polypropylene fiber concrete containing recycled aggregate. *Constr. Build. Mater.* **2020**, *241*, 118010. [CrossRef]
19. Kizilkanat, A.B.; Kabay, N.; Akyüncü, V.; Chowdhury, S.; Akça, A.H. Mechanical properties and fracture behavior of basalt and glass fiber reinforced concrete: An experimental study. *Constr. Build. Mater.* **2015**, *100*, 218. [CrossRef]
20. Zong, S.; Liu, Z.; Li, S.; Lu, Y.; Zheng, A. Stress-strain behaviour of steel-fibre-reinforced recycled aggregate concrete under axial tension. *J. Clean. Prod.* **2021**, *278*, 123248. [CrossRef]
21. Das, C.S.; Dey, T.; Dandapat, R.; Mukharjee, B.B.; Kumar, J. Performance evaluation of polypropylene fibre reinforced recycled aggregate concrete. *Constr. Build. Mater.* **2018**, *189*, 649–659. [CrossRef]
22. Ashraf, M.J.; Idrees, M.; Akbar, A. Performance of silica fume slurry treated recycled aggregate concrete reinforced with carbon fibers. *J. Build. Eng.* **2023**, *66*, 105892. [CrossRef]
23. Gu, L.; Liu, Y.; Zeng, J.; Zhang, Z.; Pham, P.N.; Liu, C.; Zhuge, Y. The synergistic effects of fibres on mechanical properties of recycled aggregate concrete: A comprehensive review. *Constr. Build. Mater.* **2024**, *436*, 137011. [CrossRef]
24. Ahmed, W.; Lim, C.W. Multicriteria performance assessment of sustainable recycled concrete produced via hybrid usage of basalt, polypropylene and glass fiber. *Constr. Build. Mater.* **2023**, *397*, 132462. [CrossRef]
25. Htet, P.; Chen, W.; Hao, H.; Shaikh, F. Influence of micro basalt and recycled macro polypropylene hybrid fibre on physical and mechanical properties of recycled aggregate concrete. *J. Build. Eng.* **2023**, *76*, 107083. [CrossRef]
26. Lei, B.; Li, W.; Liu, H.; Tang, Z.; Tam, V.W. Synergistic effects of polypropylene and glass fiber on mechanical properties and durability of recycled aggregate concrete. *Int. J. Concr. Struct. Mater.* **2020**, *14*, 37. [CrossRef]
27. Tariq, Z.; Bahadori-Jahromi, A.; Room, S. Sustainable incorporation of recycled tire steel and textile fibers as a hybrid mix in concrete. *Sustainability* **2026**, *18*, 786. [CrossRef]
28. Ali, B. Development of environment-friendly and ductile recycled aggregate concrete through synergetic use of hybrid fibers. *Environ. Sci. Pollut. Res.* **2022**, *29*, 34452–34463. [CrossRef]
29. He, W.; Kong, X.; Fu, Y.; Zhou, C.; Zheng, Z. Experimental investigation on the mechanical properties and microstructure of hybrid fiber reinforced recycled aggregate concrete. *Constr. Build. Mater.* **2020**, *261*, 120488. [CrossRef]
30. Adamu, M.; Sapkota, S.C.; Das, S.; Saha, P.; Ibrahim, Y.E. An explainable boosting-based ensemble machine learning model for predicting the properties of date palm fiber reinforced concrete. *Sustain. Chem. Pharm.* **2025**, *44*, 101949. [CrossRef]
31. Zhang, S.; Chen, W.; Xu, J.; Xie, T. Use of interpretable machine learning approaches for quantificationally understanding the performance of steel fiber-reinforced recycled aggregate concrete: From the perspective of compressive strength and splitting tensile strength. *Eng. Appl. Artif. Intell.* **2024**, *137*, 109170. [CrossRef]

32. Ahmed, A.H.A.; Jin, W.; Ali, M.A.H. Prediction of compressive strength of recycled concrete using gradient boosting models. *Ain Shams Eng. J.* **2024**, *15*, 102975. [CrossRef]
33. Golafshani, E.; Khodadadi, N.; Ngo, T.; Nanni, A.; Behnood, A. Modelling the compressive strength of geopolymer recycled aggregate concrete using ensemble machine learning. *Adv. Eng. Softw.* **2024**, *191*, 103611. [CrossRef]
34. Zhao, N.; Zhang, H.; Xie, P.; Chen, X.; Wang, X. Prediction of compressive strength of multiple types of fiber-reinforced concrete based on optimized machine learning models. *Eng. Appl. Artif. Intell.* **2025**, *152*, 110714. [CrossRef]
35. Yang, L.; Qi, C.; Lin, X.; Li, J.; Dong, X. Prediction of dynamic increase factor for steel fibre reinforced concrete using a hybrid artificial intelligence model. *Eng. Struct.* **2019**, *189*, 309–318. [CrossRef]
36. Alarfaj, M.; Qureshi, H.J.; Shahab, M.Z.; Javed, M.F.; Arifuzzaman, M.; Gamil, Y. Machine learning based prediction models for spilt tensile strength of fiber reinforced recycled aggregate concrete. *Case Stud. Constr. Mater.* **2024**, *20*, e02836. [CrossRef]
37. Dahish, H.A.; Alkharisi, M.K. Predicting the properties of polypropylene fiber recycled aggregate concrete using response surface methodology and machine learning. *Buildings* **2025**, *15*, 3709. [CrossRef]
38. Zhang, L.; Li, X.; Li, C.; Zhao, J.; Cheng, S. Mechanical properties of fully recycled aggregate concrete reinforced with steel fiber and polypropylene fiber. *Materials* **2024**, *17*, 1156. [CrossRef] [PubMed]
39. Alabduljabbar, H.; Farooq, F.; Alyami, M.; Hammad, A.W. Assessment of the split tensile strength of fiber reinforced recycled aggregate concrete using interpretable approaches with graphical user interface. *Mater. Today Commun.* **2024**, *38*, 108009. [CrossRef]
40. Zheng, Y.; Zhuo, J.; Zhang, P.; Ma, M. Mechanical properties and meso-microscopic mechanism of basalt fiber-reinforced recycled aggregate concrete. *J. Clean. Prod.* **2022**, *370*, 133555. [CrossRef]
41. Gao, D.; Ji, D.; Gu, Z.; Yan, H.; Zhang, Y. Workability and mechanical properties analysis of hybrid fibers reinforced self-compacting concrete incorporating recycled aggregates based on acoustic emission technique. *Structures* **2023**, *51*, 1722–1741. [CrossRef]
42. Meesala, C.R. Influence of different types of fiber on the properties of recycled aggregate concrete. *Struct. Concr.* **2019**, *20*, 1656–1669. [CrossRef]
43. Ali, B.; Qureshi, L.A. Influence of glass fibers on mechanical and durability performance of concrete with recycled aggregates. *Constr. Build. Mater.* **2019**, *228*, 116783. [CrossRef]
44. Daoudi, S.; Anouar Zouaoui, C.M.; El-Mezouar, M.C.; Taleb, N. Parallelization of the K-Means Clustering Algorithm. *Ingénierie Des Systèmes D'information* **2021**, *26*, 59–66. [CrossRef]
45. Nti, I.K.; Nyarko-Boateng, O.; Aning, J. Performance of machine learning algorithms with different K values in K-fold cross-validation. *Int. J. Inf. Technol. Comput. Sci.* **2021**, *13*, 61–71.
46. Ahmed, A.A.M. Prediction of dissolved oxygen in Surma River by biochemical oxygen demand and chemical oxygen demand using the artificial neural networks (ANNs). *J. King Saud Univ.-Eng. Sci.* **2017**, *29*, 151–158. [CrossRef]
47. Chen, T.; Guestrin, C. XGBoost: A Scalable Tree Boosting System. In *KDD'16: Proceedings of the 22nd ACM SIGKDD International Conference on Knowledge Discovery and Data Mining*; Cornell University: Ithaca, NY, USA, 2016.
48. Priya, G.V.; Ganguly, S. Multi-swarm surrogate model assisted PSO algorithm to minimize distribution network energy losses. *Appl. Soft Comput.* **2024**, *159*, 111616. [CrossRef]
49. Wang, Y.; Wang, Z.; Luo, Y. A hybrid carbon price forecasting model combining time series clustering and data augmentation. *Energy* **2024**, *308*, 132929. [CrossRef]
50. Alsattar, H.A.; Zaidan, A.A.; Zaidan, B.B. Novel meta-heuristic bald eagle search optimisation algorithm. *Artif. Intell. Rev.* **2020**, *53*, 2237–2264. [CrossRef]
51. Gueymard, C.A. A review of validation methodologies and statistical performance indicators for modeled solar radiation data: Towards a better bankability of solar projects. *Renew. Sustain. Energy Rev.* **2014**, *39*, 1024–1034. [CrossRef]
52. Li, M.; Tang, X.; Wu, W.; Liu, H. General models for estimating daily global solar radiation for different solar radiation zones in mainland China. *Energy Convers. Manag.* **2013**, *70*, 139–148. [CrossRef]